Turbulent Bursts in Couette–Taylor Flow

Philip S. Marcus

University of California, Berkeley, CA 94720, USA

Abstract. A new mathematical model for turbulent bursts in the three–dimensional flow between concentric, rotating cylinders (Couette–Taylor flow) is presented. Within a certain flow regime, if the parameters are held fixed, the flow oscillates in time between a spatially laminar phase (temporally chaotic Interpenetrating Spiral Vortex flow) and a turbulent phase. Our mathematical model is based on our previously published [1] fully–resolved, direct numerical simulation (i.e., using the Navier–Stokes equation with no turbulence modeling). From these simulations we developed a physical model [2] that breaks up the cycle into four physical processes: (1) the flow sets up a laminar equilibrium of vortices (Interpenetrating Spiral Vortex flow); (2) the equilibrium becomes unstable to a linear Floquet mode which grows exponentially from random, small initial conditions; (3) this mode acts as a finite–amplitude trigger for a shear–driven instability which results in large–amplitude, space–filling turbulence; and (4) after the turbulence exhausts the energy stored in the mean azimuthal component of the flow, dissipation causes it to collapse and the cycle repeats. Here, we derive a mathematical model from the Navier–Stokes equations using approximations based on the physical model. We show how well the model agrees with the numerically computed velocities, how it explains correlations and other properties of the numerically computed fields, and how it makes predictions that could be tested in future experiments.

1 Introduction

We present a new mathematical model for cyclic turbulent bursts in a fluid flow. Our mathematical model is based on direct numerical simulations of Couette–Taylor flows, i.e., those between two independently rotating, concentric cylinders, and a physical model we developed for these flows [1, 2]. In Couette–Taylor flow there is a regime in which, while holding all of the parameters fixed, the flow oscillates in time between a laminar, spatially coherent phase and a turbulent one. A single cycle of transition from laminar flow to turbulence and re–laminarization is called a 'burst cycle'. The laminar flow has coherent structures with long length scales (of order the system size) and long time scales; whereas the turbulence has no easily recognizable structure and has short length and time scales (~ 0.1 the laminar scales).

Turbulent bursts in Couette–Taylor flow were experimentally observed by Swinney and co–workers [2] who found persistent burst cycles that were approximately periodic in time. Numerical simulations of this flow and a physical model for it were presented by Coughlin & Marcus [1] and Coughlin *et al.* [2]. The latter paper also contains a description of the laboratory experiments and their comparison with the numerical simulations and our physical model.

J.L. Lumley (Ed.): LNP 566, pp. 183–200, 2001.

This paper is organized as follows: first we review the phenomenology and observations of the burst cycles. We then summarize the simulations and physical model, including the model's verification and its predictions. We then introduce our new mathematical model, describe its characteristics and its predictions that are testable by laboratory experiments and numerical simulation.

2 Review of Turbulent Burst Cycles in the Couette–Taylor System

The radius and aspect ratios of the Couette–Taylor system are $\eta = a/b$ and $\Gamma = H'/(b-a)$, where H', a, and b are the height and inner and outer radii of the cylinders. The control parameters are the ratio of the angular velocities of the outer and inner cylinders $\mu \equiv \Omega_b/\Omega_a$ and the Reynolds number $R \equiv (b-a)|b\Omega_b - a\Omega_a|/\nu$ where ν is the kinematic viscosity. We choose the unit of density to be the constant density of the fluid, length to be $(b-a)$, and velocity to be $a|\Omega_a|$. For $R < R_c$ the base flow of the system is Circular Couette flow, $\mathbf{V}_{\rm cc}(r)$ which in the limit of infinite Γ is only in the azimuthal direction. The laboratory experiments in which bursts were observed had $\Gamma \geq 26$, $\eta \equiv 0.799$, and $\mu \equiv -2.797$, and we use the latter two values throughout this paper. For $\Gamma \to \infty$, $\mathbf{V}_{\rm cc}$ is linearly, inviscidly, and centrifugally unstable to the formation of Taylor vortices in regions where $dL^2/dr < 0$, where $L(r)$ is the angular momentum per unit mass of the fluid. When $\mu < 0$, the nodal surface r^* is defined such that $v_\phi(r = r^*, \phi, z, t) = 0$ where v_ϕ is the azimuthal velocity. When $r < r^*$ (defined as the 'inner region'), $dL^2/dr < 0$, and the flow is centrifugally unstable; when $r > r^*$ (the 'outer region'), $dL^2/dr > 0$, and the flow is stable. The primary bifurcation in this system is from $\mathbf{V}_{\rm cc}$ to a flow that contains spiral Taylor vortices that are confined to $r < r^*$.

In the numerical simulations when R is increased above the critical value R_c, $\mathbf{V}_{\rm cc}$ goes unstable to eigenmodes of the form $\mathbf{f}(r)e^{i(2\pi z/\lambda + m(\phi - ct))} + \text{c.c.}$, where $\lambda > 0$ and c.c. means 'complex conjugate'. For $\mu < 0$, the critical value for m for the bifurcation has $m_c \neq 0$ and $Real\{c\} \neq 0$. Thus the primary unstable eigenmode is a uniformly rotating spiral. Modes with $m > 0$ ($m < 0$) are left– (right–) handed. Left and right–handed spiral eigenmodes are degenerate with the same $\mathbf{f}(r)$, growth rates and critical values R_c, λ_c and $|m_c|$. For the μ and η of the laboratory experiments, $R_c = 2116.6$, $\lambda_c = 1.0856$, $|m_c| = 4$, and $Real\{c\} = 0.334\Omega_a$. For $R > R_c$, the most unstable eigenmodes have $Real\{c\} \simeq 0.3\Omega_a$, and $Real\{c\}$ is approximately independent of m, λ, μ and R. The eigenmode has its peak value at $r^\dagger < r^*$ with $|\mathbf{V}_{\rm cc}(r^\dagger)/r^\dagger| \simeq Real\{c\}$. This implies that the modes rotate with the approximate speed of the local azimuthal flow, which for $r^\dagger < r^*$, is always in the same direction as the inner cylinder. Spiral eigenmodes are supercritical bifurcations of $\mathbf{V}_{\rm cc}$. For R slightly greater than R_c, they evolve to fully nonlinear Spiral Vortex flows $\mathbf{V}_{\rm sv}$ with form

$$\mathbf{V}_{\rm sv}\big(r, 2\pi z/\lambda + m(\phi - ct)\big) = \sum_{n=\infty}^{\infty} \mathbf{A}_n(r) e^{in[2\pi z/\lambda + m(\phi - ct)]}. \qquad (1)$$

The sign of the helicity of the equilibrium flow depends on initial conditions, and, once established, a spiral of one helicity is stable to perturbations of the opposite helicity. At $R = 1.04R_c$ the eigenmodes of $\mathbf{V}_{cc}$ with $|m| \neq 4$ are stable, but all eigenmodes with $1.34 \geq \lambda \geq 0.820$ and $|m| = 4$ are unstable. The degeneracy in λ does not lead to mode competition; numerical experiments (which are forced to have axial periodicity $H = 4\lambda_c$) initialized with a sum of left– and right–handed eigenmodes with axial wavelengths of $H/2$, $H/3$, $H/4$ and $H/5$ converge to Spiral Vortex flow with a single helicity as in equation (1). The final Spiral Vortex flow has $m = 4$ (or $m = -4$, but not both) and $\lambda = H/4$. Spiral Vortex flow consists of a pair of counter-rotating vortices localized in the centrifugally unstable inner region. The circulation due to the vortices mixes the fluid in the inner region and reduces the gradient of the mean velocity $\bar{V}(r)$

$$\bar{V}(r) \equiv \frac{1}{2\pi H} \int_0^H \int_0^{2\pi} v_\phi \, dz \, d\phi. \tag{2}$$

In the outer region, the flow remains almost two-dimensional and similar to $\mathbf{V}_{cc}(r)$. In the numerical experiments at $R > 1.04R_c$, $\mathbf{V}_{sv}$ becomes unstable to a flow with turbulent burst cycles. During the laminar phase of the cycle the flow strongly resembles Interpenetrating Spiral Vortex flow $\mathbf{V}_{isv}$. A pure $\mathbf{V}_{isv}$ flow is a chaotic equilibrium first observed in a different parameter regime by Andereck *et al.* [3]. It contains multiple spiral vortices with different helicities, (i.e., in numerical calculations $\mathbf{V}_{isv}$ flow has multiple values of m and λ in equation (1)), making it temporally chaotic but spatially laminar. During the turbulent phase of the burst cycle the turbulence is *space–filling*, and the flow has no recognizable structure.

Although our numerical simulations resolve the flow and are direct (i.e., they are solutions to the Navier–Stokes equation with no turbulence modeling terms), they do use an important approximation. The no–slip boundary conditions of the axial end plates are replaced by an assumption of axial periodicity H. This leads to some differences, which we argued [1, 2] are unimportant for the study of turbulent bursts, but which we now describe for completeness. In the laboratory flow with finite Γ, the primary bifurcation from $\mathbf{V}_{cc}$ is different than it is in the numerical simulations. The flow goes unstable directly to a flow with turbulent bursts rather than to $\mathbf{V}_{sv}$. The laminar phase of the cycle is similar to the Interpenetrating Spiral Vortex flow of the numerical simulations, but the turbulent phase of the cycle has its turbulence spatially confined to localized 'spots'. As R increases the turbulent 'spots' become larger, and at $R > R_c''$, the turbulent phase of the burst cycle is space–filling as in the numerical simulations. The burst cycles are almost periodic in time with mean duration T. Both T and its standard deviation decrease with increasing R. Coughlin & Marcus [1] and Coughlin *et al.* [2] discuss in detail the consequences of the differences, but conclude that the flows with space–filling turbulent burst cycles in the simulations and in the laboratory experiments are essentially the same. There is good quantitative agreement between the two (e.g., the periods and standard deviations of the burst cycles at selected values of R). Moreover, two *predictions* made from

the numerical simulations (described in the next section) were subsequently verified in the laboratory experiments. Not only did these strongly suggest that the numerical simulations capture the underlying physics of the laboratory flow, but also the predictions provide the basis for our physical model of the burst cycle.

3 Physical Model

The main ideas and assumptions underlying our physical model are outlined in this section. In particular, Couette–Taylor flow with counter–rotating cylinders acts as if it contains two coupled dynamical systems. One, the 'inner region' with $a \leq r < r^*$, is centrifugally unstable, and its dynamics are well–understood by linear theory. The second system, or 'outer region', is centrifugally stable but finite–amplitude unstable to shear instabilities, which are nonlinear and create the turbulence in the burst cycle. The second main idea of the model is that the flow would remain indefinitely in its laminar phase as an Interpenetrating Spiral Vortex flow concentrated in the inner region if $\mathbf{V}_{\rm isv}$ were not linearly unstable. Its instability is a linear eigenmode, which acts as a weak 'trigger' that sets off the finite–amplitude instability in the outer region, which in turn creates the space–filling turbulent burst.

The analysis of the laminar phase is complicated due to the fact that Interpenetrating Spiral Vortex flow is chaotic. Hence in Coughlin & Marcus and Coughlin *et al.* [1, 2] we asked whether the chaos was essential to the burst cycle, or an extraneous complication. We concluded the latter, based on several numerical experiments (though it is easy to imagine different scenarios of turbulent burst cycles that *require* the laminar phase to be chaotic). Therefore to simplify our presentation here, we proceed as if the laminar phase were a $\mathbf{V}_{\rm sv}$ flow rather than an Interpenetrating Spiral Vortex flow. This is reasonable because Interpenetrating Spiral Vortex flow is always energetically dominated by a flow with only one helicity and at any instant in time always looks similar to a $\mathbf{V}_{\rm sv}$ flow.

The linear instabilities of $\mathbf{V}_{\rm sv}$ occur at $R \geq R_c{}'$ and are Floquet eigenmodes of the form

$$e^{im'(\phi - c't)} e^{i2\pi z/\lambda'} \mathbf{g}\Big(r, 2\pi z/\lambda + m(\phi - ct)\Big). \tag{3}$$

Numerically, we find their azimuthal phase speeds c' are $\sim -0.4\Omega_a$, approximately independent of the parameters m, m', H, λ and λ'. The critical R for onset of this Floquet mode is less than $1.04R_c$. The bifurcation is supercritical. (This is determined numerically by imposing a symmetry on the calculation that allows the Floquet modes to come to their nonlinear equilibria but disallows the flow to go unstable to turbulent bursts). The Floquet mode generically leads to a quasi–periodic, nonlinear, equilibrium flow (which could be stable or unstable) with form

$$\mathbf{V}_{\rm qp}(r, z, \phi, t) = \sum_{n,k} \mathbf{a}_{n,k}(r) e^{in[2\pi z/\lambda + m(\phi - ct)]} e^{ik[2\pi z/\lambda' + m'(\phi - c't)]}. \tag{4}$$

Comparing equations (1) and (4), it is seen that the unstable $\mathbf{V}_{\rm sv}$ which supercritically bifurcates to the $\mathbf{V}_{\rm qp}$ in equation (4) is

$$\mathbf{V}_{\rm sv} \simeq \sum_n \mathbf{a}_{n,0}(r) e^{in[2\pi z/\lambda + m(\phi - ct)]}. \tag{5}$$

The difference $(\mathbf{V}_{\rm qp} - \mathbf{V}_{\rm sv})$, defined as the modulation of $\mathbf{V}_{\rm sv}$ by $\mathbf{V}_{\rm qp}$, is dominated by

$$e^{im'(\phi - c't)} e^{i2\pi z/\lambda'} \sum_n \mathbf{a}_{n,1}(r) e^{in[2\pi z/\lambda + m(\phi - ct)]} \tag{6}$$

which is approximately the Floquet mode in (3). Although the $\mathbf{a}_{n,0}(r)$, i.e., the $\mathbf{V}_{\rm sv}$ component of $\mathbf{V}_{\rm qp}$, are radially localized in the 'inner region', (as are the Interpenetrating Spiral vortices); the Floquet eigenmode $\mathbf{a}_{n,1}(r)$, and associated modulation have large amplitudes near $r = r^*$ and are thus able to act as finite–amplitude perturbations to the flow in the 'outer region'. Based on this observation we argued in [1, 2] that this modulation was the trigger for the turbulent burst. We proposed that this modulation would always be present in the laboratory experiments and numerical simulations just prior to each burst (and at no other times.) This was easy to verify because the frequencies of the modulations and the radial locations of their amplitude maxima were computed numerically and looked for in the laboratory power spectra. Not only did the laboratory spectra display these frequencies, but they appeared just prior to each burst and at no other times. Direct numerical simulation shows that the flow never settles into a stable $\mathbf{V}_{\rm qp}$ state for $R > R_c''$, where R_c'' is only slightly greater than R_c'. The $\mathbf{V}_{\rm qp}$ flow whose amplitude is small and proportional to $(R - R_c')^{1/2}$ triggers the burst. We know this because if its amplitude *near the outer region* is kept artificially suppressed in the numerical calculations, then bursts do not occur, and the flow remains a laminar $\mathbf{V}_{\rm qp}$ flow.

Once triggered, the onset of the turbulent burst is abrupt and causes $O(1)$ changes in the velocity. Plots show the flow bursts everywhere into turbulence almost simultaneously. Large fluctuations occur on scales much smaller than the radii of the Interpenetrating Spiral Vortices and on time scales much less than the inner cylinder period. Figure 1 shows the numerically computed rates of the viscous dissipation of energy per unit mass $\dot{E}_{\rm diss}$ and the energy input rates into the flow per unit mass from the motors at the inner and outer cylinders $\dot{E}_{\rm a} \equiv \Gamma_a \Omega_a$ and $\dot{E}_{\rm b} \equiv -\Gamma_b \Omega_b$. In dimensionless variables

$$\dot{E}_{\rm a} = -2(\mu - \eta)^2 (1 - \eta^2)^{-1} R^{-1} d(\bar{V}/r)/dr \tag{7}$$

and

$$\dot{E}_{\rm b} = 2\mu\eta^{-3}(\mu - \eta)^2 (1 - \eta^2)^{-1} R^{-1} d(\bar{V}/r)/dr \tag{8}$$

where $\bar{V}(r,t)$ is the azimuthally and axially averaged value of the azimuthal velocity, Γ_a and Γ_b are the torques per unit mass on the fluid due to the walls, and where the derivatives in equations (7) and (8) are evaluated at the respective boundaries.

The small scales of the turbulent burst are efficient at viscously dissipating energy, and the contributions to $\dot{E}_{\rm diss}(t)$ are dominated by them; thus, $\dot{E}_{\rm diss}$ is a good signature of the turbulent phase of the burst cycle. In figure 1 it rises at onset, peaks when the turbulence is near its maximum, and drops when the turbulence collapses. One measure of the intensity of the turbulence is the ratio of the average value of $\dot{E}_{\rm diss}$ during the turbulent phase of the burst cycle to the rate during the laminar phase. At $R = 1.18R_c$, the ratio is 1.35, and at $R = 1.38R_c$ it is 1.60. Although the small spatial scales dissipate most of the energy, all of the energy into the flow comes from the torques at the cylinders and goes into the mean velocity $\bar{V}$. The component of energy due to $\bar{V}$ is always much greater than that due to the fluctuation $\tilde{\mathbf{v}} \equiv (\mathbf{v} - \bar{V})$. The $\tilde{\mathbf{v}}$ derives its energies from nonlinear interactions with $\bar{V}$. The total rate of change of energy of the flow is $(\dot{E}_{\rm a} + \dot{E}_{\rm b} - \dot{E}_{\rm diss})$. Figure 1 shows that $\dot{E}_{\rm b}$ and $\dot{E}_{\rm a}$ lag $\dot{E}_{\rm diss}$. The rate of energy into the flow does not begin to rise significantly until after the turbulent burst collapses. During the turbulent phase, $(\dot{E}_{\rm a} + \dot{E}_{\rm b}) < \dot{E}_{\rm diss}$, so the flow loses energy. During the turbulent phase, the energy of $\tilde{\mathbf{v}}$ grows by a factor of 20 by drawing energy from $\bar{V}$. After the collapse of the turbulence, the total flow increases its energy by decreasing $\dot{E}_{\rm diss}$ and increasing $\dot{E}_{\rm a}$ and $\dot{E}_{\rm b}$.

We had previously argued that the flow in the 'outer region' was finite–amplitude unstable [1, 2], and this argument is bolstered by the fact that when our initial–value calculations begin with a pure $\mathbf{V}_{\rm sv}$ flow superposed with small amplitude noise, the flow immediately produces a turbulent burst. (Except for this experiment, noise was never introduced into our numerical simulations of the Navier–Stokes equation; the computed bursts are turbulent, but deterministic.) Moreover, because $\eta \simeq 1$ the flow in the 'outer region' looks similar to a plane–parallel shear flow. Kim *et al.* [4] argued that any type of plane–parallel shear flow is finite–amplitude unstable when its local Reynolds number (based on the flow's cross–stream width, ν and shear at outer wall) is greater than $\sim$100. The flow in the 'outer region' meets this criterion.

Although it empirically appears that the 'outer region' is sub–critically unstable and that a finite–amplitude perturbation drives the flow to a turbulent state, we freely admit our model provides no physical explanation for finite–amplitude instability. However there appears to be no *universally* accepted *physical* explanation for finite–amplitude instabilities in shear flows, including the classic channel and pipe flows. (Models based on non–normal eigenmodes can explain why a low–dimensional transient can obtain a large amplitude before it decays, but they do not explain how the transient excites high–dimensional turbulence [5]. It should also be noted that the eigenmodes of $\mathbf{V}_{\rm cc}$ are normal and complete. Models of finite–amplitude instability based on placing trip wires in a flow to create streamwise vortices, or on numerically freezing certain modes or coherent structures are also controversial.)

In our model the reason why the turbulence decays, and the cycle begins anew is the following. The small scales excited during the turbulent phase of the burst cycle increase $\dot{E}_{\rm diss}$, but the energy input rate into the flow remains low, so the total flow loses energy. During the turbulent burst part of the cycle, the

turbulent component of the flow draws its energy from $\bar{V}(r)$ which acts as an energy reservoir. To see how this happens, note that during the laminar phase of the cycle $\bar{V}(r,t) \simeq \mathbf{V}_{\rm cc}(r)$, and $\bar{V}(r,t)$ has a large amount of differential rotation. Turbulence tends to mix and homogenize angular momentum, driving the mean flow $\bar{V}(r,t)$ towards a state with $|dL/dr| \to 0$ (far from the radial boundaries) and therefore towards one with much less differential rotation and therefore with *much less energy* than $\mathbf{V}_{\rm cc}(r)$ [2]. The energy difference between these two mean flows is the reservoir from which the turbulent burst draws its energy. Once the turbulence has extracted the available energy from $\bar{V}$, dissipation takes over, the turbulence collapses, and the flow re–laminarizes. Then the flow returns to a state similar to $\mathbf{V}_{\rm cc}$, $|dL/dr|$ increases, $\dot{E}_{\rm b}$ and $\dot{E}_{\rm a}$ increase, and the cycle repeats.

Quantitative laboratory support for our physical model comes from the fact that it predicts how the burst cycles scale with R in our direct numerical simulations of Navier–Stokes equations and in the laboratory experiments. The model predicts the mean lengths of the laminar $T_{\rm L}$, and turbulent $T_{\rm B}$ phases of the burst cycle scale independently. According to our physical model, if the turbulent burst is triggered when the Floquet mode reaches a critical amplitude α_c, and if the Floquet mode has growth rate β, then $T_{\rm L} = 1/\beta\langle\langle \log \alpha_c/\alpha_0 \rangle\rangle$, where the initial amplitude of the eigenmode α_0 is assumed to be a random variable independent of R_c', where R_c' is the critical R for onset of the Floquet mode. Double angle brackets indicate ensemble averaging over α_0. Generically $\beta \sim (R - R_c')$ and α_c is independent of $(R - R_c')$, so $T_{\rm L} \sim (R - R_c')^{-1}$. On the other hand, there is no reason why the time it takes for the turbulence of the burst to exhaust the energy stored in $\bar{V}$ should depend on $(R - R_c')$, so $T_{\rm B}$ should be independent of $(R - R_c')$. Both of these predictions have been confirmed in the laboratory [1, 2].

4 The Mathematical Model

In summary, the physical model ascribes four parts to the burst cycle: (1) the flow sets up a laminar equilibrium of vortices (either $\mathbf{V}_{\rm sv}$ or Interpenetrating Spiral Vortex flow); (2) the equilibrium becomes unstable to a linear Floquet mode which grows exponentially from random, small initial conditions; (3) *via* unknown (at least, to us) physics the Floquet mode triggers a finite–amplitude instability in the shear flow in the 'outer region', resulting in space–filling turbulence; and (4) after exhausting the energy stored in $\bar{V}$, small–scale dissipation causes the turbulence to collapse and the cycle repeats.

To make further progress and new predictions, it is useful to translate the physical model into a mathematical one. Our model will have three, coupled ordinary–differential equations. This appears to violate our underlying belief that the third step of the cycle, the finite–amplitude instability, is not understood. It also appears to violate our belief that turbulent bursts are inherently high dimensional and cannot be described by low–order mathematics. These points are reconciled below.

4.1 Derivation of Model Equations

The dynamical variables of our model are E, $\mathcal{E}$ and ε which are, respectively, the energies per unit mass of the mean flow $\bar{V}(r,t)$, the turbulent component of the flow (which consists of many Fourier modes) and the energy of the Floquet trigger mode. By multiplying the Navier–Stokes equation by $\bar{V}(r,t)$ and integrating over the spatial domain we obtain (for clarity we revert to using dimensional variables unless specified otherwise):

$$dE/dt = -\chi + (\dot{E}_a + \dot{E}_b) - D, \tag{9}$$

where

$$E \equiv \int_a^b \bar{V}^2 \, r \, dr/(b^2 - a^2), \tag{10}$$

D is the rate at which energy is viscously dissipated from E:

$$D \equiv 2\nu \int_a^b |\nabla \times \bar{V}\,\hat{\phi}|^2 \, r dr/(b^2 - a^2), \tag{11}$$

$\hat{\phi}$ is the unit vector in the azimuthal direction, $(\dot{E}_a + \dot{E}_b)$ is the energy input rate from the motors given by equations (7)–(8), and χ is the rate at which energy is transferred nonlinearly from E to the other modes:

$$\chi \equiv -\int_a^b r dr \int_0^{2\pi} d\phi \int_0^H dz \, \bar{V}\hat{\phi} \cdot [(\mathbf{v} \cdot \nabla)\mathbf{v}]/\pi H(b^2 - a^2) \tag{12}$$

$$= -\int_a^b r dr \int_0^{2\pi} d\phi \int_0^H dz \, \bar{V}\hat{\phi} \cdot [(\tilde{\mathbf{v}} \cdot \nabla)\tilde{\mathbf{v}}]/\pi H(b^2 - a^2). \tag{13}$$

Note that the motors only drive energy into the mean flow; all other modes obtain their energy from the mean flow via the χ term. The velocity that makes up the turbulent phase is almost equal to $\tilde{\mathbf{v}}$. (The modes that make up the Interpenetrating Spiral Vortices and the Floquet mode are part of neither $\bar{V}(r,t)$ nor the turbulent phase.) However during the turbulent phase, $\mathcal{E}$ is much greater than the energy of the spiral modes and trigger, so $d\mathcal{E}/dt$ is well–approximated by multiplying the Navier–Stokes equation by $\tilde{\mathbf{v}}$ and integrating over the spatial domain:

$$d\mathcal{E}/dt = \chi - \mathcal{D} \tag{14}$$

where $\mathcal{D}$ is the rate at which energy is viscously dissipated from $\mathcal{E}$,

$$\mathcal{D} \equiv \nu \int_a^b r dr \int_0^{2\pi} d\phi \int_0^H dz |\nabla \times \tilde{\mathbf{v}}|^2/\pi H(b^2 - a^2). \tag{15}$$

Note that in figure 1 we plotted the rate of energy dissipation. This obeys $\dot{E}_{\text{diss}} = D + \mathcal{D}$.

We now approximate the terms in equations (9)–(15). We want to write them in terms of E, $\mathcal{E}$ R, μ and η. In dimensionless form equations (11) and (15) become

$$D = C_1 E/R \tag{16}$$

$$\mathcal{D} = C_2\mathcal{E}/R \tag{17}$$

where $C_1 \equiv (\eta-\mu)/\eta L_1^2$ and $C_2 \equiv (\eta-\mu)/\eta L_2^2$, and where the definitions of the dimensionless lengths L_1 and L_2 are defined:

$$L_1^2 \int_{\eta/(1-\eta)}^{1/(1-\eta)} (\nabla \times \bar{V}\hat{\phi})^2 r dr \equiv E \int_{\eta/(1-\eta)}^{1/(1-\eta)} r dr \tag{18}$$

and

$$L_2^2 \int_{\eta/(1-\eta)}^{1/(1-\eta)} r dr \int_0^{2\pi} d\phi \int_0^{H/(b-a)} dz (\nabla \times \tilde{\mathbf{v}})^2 \equiv \mathcal{E} 2\pi (H/(b-a)) \int_{\eta/(1-\eta)}^{1/(1-\eta)} r dr. \tag{19}$$

That is, L_1 and L_2 are the characteristic lengths over which $\bar{V}$ and $\tilde{\mathbf{v}}$ change. From plots of $\bar{V}(r)$ as functions of r [1], it appears that $L_1 \simeq 0.36$ ($\sim 1/3$ the gap width) which gives $C_1 = 34$. A better value, determined from the full numerical simulations of the Navier–Stokes equation, agrees with this value of C_1 to within 10% (see §4.4). A reasonable estimate for L_2 based on the observed size of the small scales during the turbulent phase is $L_2 \simeq 0.1$. A better value inferred from the full numerical simulations is $L_2 \simeq 0.078$, which gives $C_2 = 745$. (See § 4.4.) None of the qualitative features of the model depends strongly on the exact values of C_1 or C_2 and neither appear to be strongly dependent on R, E or $\mathcal{E}$. (Note, the turbulent burst is not of sufficient duration for the turbulence to be fully developed such that $\mathcal{D} \propto \mathcal{E}^{3/2}$.)

A casual examination of equation (13) suggests that χ should scale as $E^{1/2}\mathcal{E}$, but instead we argue (in dimensionless form)

$$\chi = C_3 E \mathcal{E}^{1/2}. \tag{20}$$

(We show below that if $\chi \propto E^{1/2}\mathcal{E}$, then the dynamics predicted by the model are qualitatively dissimilar to those found from the direct numerical simulations of the Navier–Stokes equations. Furthermore the direct simulations qualitatively confirm equation (20).) We heuristically 'derive' equation (20) from angular momentum conservation where the angular momentum per unit volume in a shell at radius r is $J \equiv \rho r \bar{V}$, and its radial flux is F:

$$\partial J(r,t)/\partial t = -\frac{1}{r}\frac{\partial}{\partial r} rF. \tag{21}$$

The component of F due to advection is

$$F_A(r,t) \equiv \langle \tilde{v}_r \rangle \langle \rho r \tilde{v}_\phi \rangle c \tag{22}$$

where c is the correlation between $\tilde{v}_r$ and $\tilde{v}_\phi$. Angle brackets indicate an rms–average over ϕ and z. There is a second contribution to F from diffusion which is $O(\nu)$. Multiplying equation (21) by $J/\rho^2 r^2$, integrating over the volume, and dividing by the volume, we obtain

$$dE/dt = -2 \int_a^b dr\, J \left(\frac{d(rF_A)}{dr} \right) \Big/ \rho^2 r^2 (b^2 - a^2) + O(\nu) \tag{23}$$

where we identify the right–hand side of equation (23) (excluding the contribution from the $O(\nu)$ terms which represent the energy input from the motors and the dissipation terms) as the change in E due to the advective term or $-\chi$. Integrating equation (23) by parts we obtain

$$\chi = -2 \int_a^b dr\, r\, F_A \left(\frac{d(J/r^2)}{dr} \right) \Big/ \rho^2 (b^2 - a^2) \tag{24}$$

where we use the fact that $F_A = 0$ at the radial boundaries. We now define the mixing length Λ:

$$F_A \equiv -\Lambda \langle \tilde{v}_r \rangle \, dJ/dr. \tag{25}$$

To this point in the derivation of equation (20) we have made no approximations other than define the mixing length.

We now approximate $J(r,t)$ as a Taylor expansion about r^* and use the fact that $J(r^*,t) \simeq 0$:

$$J(r,t) \simeq \rho s(t)(r - r^*). \tag{26}$$

Equation (26) fits the numerical simulations reasonably well except near the radial boundaries [1]. Due to the fact that the radial gap is small, equation (26) implies

$$d(J/r^2)/dr \simeq \rho s(t)/r^2 \tag{27}$$

Equations (24) – (27) yield

$$\chi \propto \langle \tilde{v}_r \rangle \Lambda s^2(t) \tag{28}$$

where the proportionality constant is positive and depends only on the geometry of the Couette apparatus (and not on R or other flow parameters if we assume that r^* is approximately constant). The value of E is determined by integrating J/r over the domain, so using equation (26) it is easy to show that $s^2 \propto E$ (the errors due to the poor approximation of J at the boundaries is negligible), and the proportionality constant is positive and depends only on the Couette apparatus geometry. The full numerical simulations also show that there is a nearly equi–partition of energy among the components of $\tilde{\mathbf{v}}$ and therefore that $\langle \tilde{v}_r \rangle \propto \mathcal{E}^{1/2}$. Using $s^2 \propto E$ and $\langle \tilde{v}_r \rangle \propto \mathcal{E}^{1/2}$ in equation (28) yields equation (20). For the parameter values of μ and η used in this paper and the value of r^* from $\mathbf{V}_{\rm cc}$ we can calculate the geometric factors and obtain

$$C_3 \simeq 9\Lambda/(b-a). \tag{29}$$

Basing Λ on the lengths of the energy–bearing modes during the turbulent phase (and assuming they are nearly constant during that phase) we set $C_3 = 0.03$.

To approximate $(\dot{E}_a + \dot{E}_b)$ from equations (7) and (8) we need to approximate $\partial(\bar{V}/r)\partial r$ at the boundaries. Assuming that equation (26) is valid in the interior of the flow and that there are boundary layers with thicknesses L_a and L_b, implies at $r = a$:

$$\partial(\bar{V}/r)\partial r = [s(t)(a + L_a - r^*)/(a + L_a)^2 \; - \Omega_a]/L_a \tag{30}$$

with a similar expression at $r = b$. Assuming that $L_a/a \ll 1$, using equations (7), (8), and (30), and approximating r^* with its value in $\mathbf{V}_{cc}$, gives (in dimensionless form)

$$\dot{E}_a + \dot{E}_b = (C_5 - C_4\sqrt{E})/R \tag{31}$$

where C_4 and C_5 are dimensionless constants that depend on the values of L_a and L_b. It is more useful to define a new constant E_0 such that $C_4\sqrt{E_0} + C_1 E_0 \equiv C_5$ and use E_0 rather than C_5 as a parameter in our model,

$$\dot{E}_a + \dot{E}_b = [C_4(\sqrt{E_0} - \sqrt{E}) + C_1 E_0]/R. \tag{32}$$

Based on the numerical simulations [1], we expect $L_a \simeq L_b \simeq 0.16(b-a)$ (which we treat as constants, independent of R, E and $\mathcal{E}$). A better estimate of their values and direct measurements of the values of E_0 and C_4 can be made using the methods described in §4.4. However those estimates and measurements are consistent with our choices for L_a and L_b and give values $E_0 \simeq 1.67$ and $C_4 \simeq 211$. Combining equations (9), (14), (16), (17) (20) and (32) we obtain our model:

$$dE/dt = -C_3 E\mathcal{E}^{1/2} + [C_4(\sqrt{E_0} - \sqrt{E}) + C_1(E_0 - E)/]R \tag{33}$$

$$d\mathcal{E}/dt = C_3 E\mathcal{E}^{1/2} - C_2\mathcal{E}/R. \tag{34}$$

4.2 Finite–Amplitude Effects

Clearly, one of the two fixed points of these two equations is $E = E_0$ and $\mathcal{E} = 0$. The parameter E_0 is the value of E during the laminar phase, which is easily determined from simulations (see §4.4). This fixed point in equations (33) - (34) is linearly unstable. The other fixed point has values of E_f and $\mathcal{E}_f$, is a solution of a fourth–order equation, and (even without knowing the solution in closed form) it can be shown that it is linearly stable and has $E_f < E_0$. It can also be shown that E_f decreases with increasing R, while $\mathcal{E}_f$ increases.

Equations (33) and (34) are not yet complete because they fail to incorporate the unknown physics of the finite–amplitude instability of the shear flow. Our main assumption about the finite–amplitude instability is that when ε *or* $\mathcal{E}$ exceed their critical values ε_c and $\mathcal{E}_c$, the nonlinear energy transfer term χ is 'on', otherwise it is 'off' (i.e., $\chi \equiv 0$). This is consistent with the numerical simulations which show that the term is only 'on' during part of the turbulent burst phase. This idea can be incorporated into equations (33) and (34) by replacing C_3 with C_3 multiplied by $\mathcal{H}$

$$dE/dt = -C_3\mathcal{H}E\mathcal{E}^{1/2} + [C_4(\sqrt{E_0} - \sqrt{E}) + C_1(E_0 - E)/]R \tag{35}$$

$$d\mathcal{E}/dt = C_3\mathcal{H}E\mathcal{E}^{1/2} - C_2\mathcal{E}/R \tag{36}$$

where $\mathcal{H} = 1$ if either $\mathcal{E} > \mathcal{E}_c$ or if $\varepsilon > \varepsilon_c$; otherwise $\mathcal{H} = 0$. We write an equation for $\varepsilon(t)$ by noting that when the flow is close to $\mathbf{V}_{sv}$ flow, the Floquet mode is unstable and ε grows exponentially with e–folding time $1/2\beta$. When the flow is turbulent and far from $\mathbf{V}_{sv}$ flow, the growth should stop, and the Floquet

mode should decay with its viscous time scale which is approximately R/C_1. (We used C_1 because the characteristic length scales of the Floquet mode and $\bar{V}$ are similar.) If we assume that the flow is far from $\mathbf{V}_{\rm sv}$ when $E < \gamma E_0$, where $0 < \gamma < 1$, then

$$\partial\varepsilon/\partial t = [(2\beta + C_1/R)\, h(E - \gamma E_0) - C_1/R]\varepsilon \tag{37}$$

where $h(E - \gamma E_0)$ is the Heaviside function equal to 0 for negative arguments and 1 for positive arguments. Note that in our model E is never greater than E_0 – see below. We have found that our model is fairly insensitive to the value of γ, and $\gamma = 0.9$ works well. Also note that we add a small, positive, random amplitude $\alpha_0 \ll \varepsilon_c$ to ε at the beginning of each burst cycle (i.e., everytime the Heaviside function h switches from 0 to 1). This has the effect of making the 'initial condition' of the trigger stochastic for each burst cycle; otherwise, all burst cycles would be identical.

When $\mathcal{H} = 0$, equations (35) and (36) have only one fixed point: $E = E_0$ and $\mathcal{E} = 0$. It is linearly stable (and, in fact, globally attracting). Note that if $\mathcal{E}_f > \mathcal{E}_c$, the turbulence is self-sustaining and the burst cycles stop.

Although the use of $\mathcal{H}$ in equations (35) – (36) is a crude way of parameterizing our ignorance of the physics of the finite–amplitude instability, we now show that the equations are nonetheless useful in explaining a large number of the properties of the burst cycles.

4.3 Properties of the Model

A single burst cycle computed with equations (35) – (37) with $\gamma = 0.999$ and no noise in equation (37) is shown in figure 2 for parameter values similar to those discussed above. The cycle begins with χ 'off' or $\mathcal{H} = 0$ near the stable laminar fixed point with $E = E_0$ and $\mathcal{E} = 0$ labeled **a** in figures 1 and 2. This point corresponds to $\mathbf{V}_{\rm sv}$ flow which has an unstable Floquet trigger mode whose energy ε grows from its initial value as $e^{2\beta t}$. While the flow is near this fixed point (or *any* fixed point) $\dot{E}_{\rm diss} \simeq (\dot{E}_{\rm a} + \dot{E}_{\rm b})$, which is illustrated in figure 1 as locations where the dashed and solid curves cross.

Henceforth we shall define and label as **a** all points that correspond to a crossing of the two curves in figure 1 that occur with low values of $\dot{E}_{\rm diss}$ and label with **c** those crossings that occur with high values of $\dot{E}_{\rm diss}$.

When $\varepsilon > \varepsilon_c$, χ switches 'on', the fixed point at **a** becomes unstable and the solution in figure 2 moves from **a** to **b**, increasing $\mathcal{E}$ and decreasing E. During this time $\dot{E}_{\rm diss}$ and $\mathcal{E}$ increase rapidly while $(\dot{E}_{\rm a} + \dot{E}_{\rm b})$ (which depends only on the square root of E) increases only slowly, so $\dot{E}_{\rm diss} > (\dot{E}_{\rm a} + \dot{E}_{\rm b})$ in figure 1. At some point along the path from **a** to **b**, the flow becomes sufficiently far from $E = E_0$ that it no longer looks like a $\mathbf{V}_{\rm sv}$ flow. Thus the base flow for the Floquet trigger no longer exists and ε decays to zero. The χ term remains 'on' because $\mathcal{E} > \mathcal{E}_c$. $\dot{E}_{\rm diss}$ reaches its maximum value $\dot{E}_{\rm diss}^{\rm max}$ at **b**. Henceforth points **b** are defined as the locations of the maxima of $\dot{E}_{\rm diss}$. For large values of $\mathcal{E}$, $\dot{E}_{\rm diss} \simeq C_2\mathcal{E}/R$ and is independent of E; thus **b** is very close to the point in

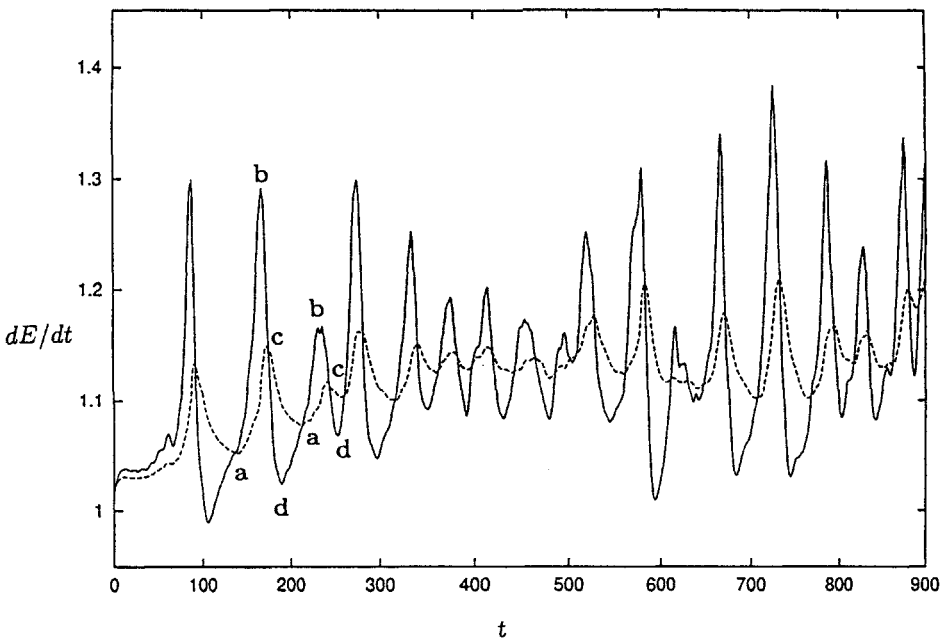

FIGURE 1 – Energy dissipation $\dot{E}_{\rm diss}$ (shown with a solid curve) by viscosity and the energy input rate from the torques at the two radial boundaries ($\dot{E}_{\rm b} + \dot{E}_{\rm a}$) (broken curve) as functions of time. The values are computed for the parameter values discussed in the text using the direct numerical simulation *not* the model equations. For each cycle the maxima and minima of the solid curve are defined as **b** and **d** respectively. The locations where the two curves cross with low values of $\dot{E}_{\rm diss}$ are defined as **a** and where they cross at large values of $\dot{E}_{\rm diss}$ are defined as **c**. These locations are shown for two contiguous cycles.

figure 2 where $\mathcal{E}$ reaches its maximum value. (The model predicts that $\mathcal{E}$ reaches its maximum value just after **b**.) From this point to **c**, both $\mathcal{E}$ and E decrease. The latter causes ($\dot{E}_{\rm a} + \dot{E}_{\rm b}$) (which from equation (32) is a function only of E) to continue to increase. During this time not only is $\dot{E}_{\rm diss} > (\dot{E}_{\rm a} + \dot{E}_{\rm b})$, but also $\mathcal{E}$ dissipates energy faster than it receives it from E, i.e., $C_2\mathcal{E}/R > \chi$. The solution approaches the fixed point (E_f,$\mathcal{E}_f$) labeled **c** in figure 2, but in this calculation we have set $\mathcal{E}_c$ to be slightly greater than $\mathcal{E}_f$. Thus χ turns 'off' just before the solution reaches **c**. It is then attracted back to the other fixed point at **a**. Note that the fixed point **c** in figure 2 is where E has its minimum value and therefore where ($\dot{E}_{\rm a} + \dot{E}_{\rm b}$) has its maximum. This explains (if our model is correct) why the numerical simulations in figure 1 show that during each burst cycle the points labeled **c** correspond to both the locations where the broken and solid curves cross (indicative of a fixed point if $\mathcal{E}_c \simeq \mathcal{E}_f$) *and* the (approximate) locations where ($\dot{E}_{\rm a} + \dot{E}_{\rm b}$) have maxima.

After χ turns off, $\mathcal{E}$ rapidly decays along the path **c** $\rightarrow$ **d** with time scale C_2/R. The time scale for E to return to its value of E_0 is longer. The reason

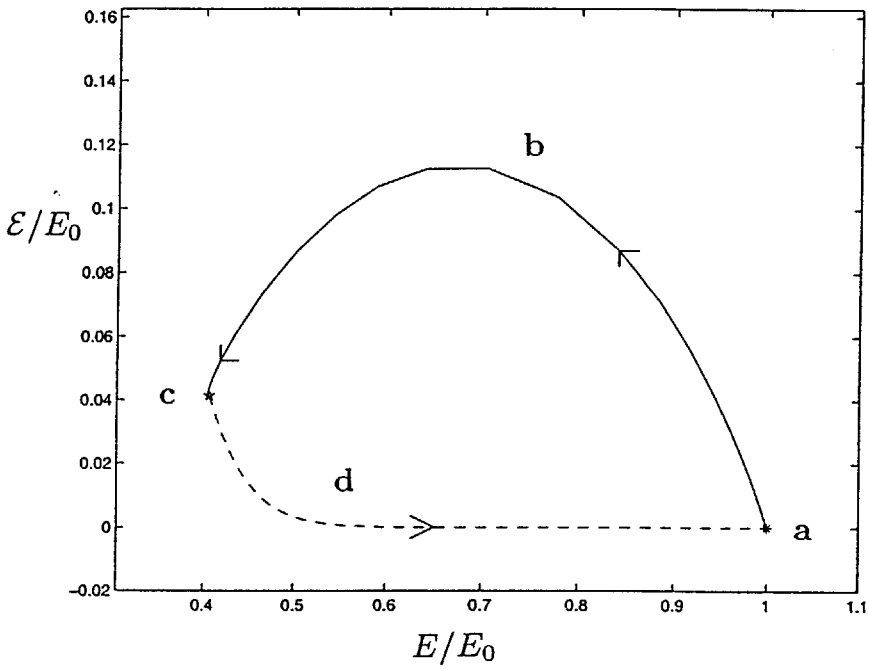

FIGURE 2 – A burst cycle computed with the model equations with the locations **a**, **b**, **c** and **d** labeled as in figure 1. The maximum value of $\mathcal{E}$ occurs on the part of the cycle **b** $\rightarrow$ **c**, close to **b**. The arrows in the figure indicate the direction of the cycle. The solid curve is computed with χ 'on' and the broken curve with χ 'off'. In this cycle the $\mathcal{E}_c$ is almost equal to (but slightly larger than) $\mathcal{E}_f$.

that $\dot{E}_{\text{diss}}$ has a minimum value (labeled and defined as **d**) prior to reaching the fixed point at **a** is due to the fact that $\mathcal{E} \simeq 0$ at both **d** and **a**, but E at **d** is less than E_0; thus $\dot{E}_{\text{diss}}$ (which is approximately equal to $C_1 E$ for small values of $\mathcal{E}$) is lower at **d** than at **a**. As the solution travels along the path from **d** to **a**, the flow reaches its maximum value of E and minimum value of $(\dot{E}_{\text{a}} + \dot{E}_{\text{b}})$ near the fixed point at E_0. Thus the crossing of the curves in figure 1 at **a** corresponds to a minimum of $(\dot{E}_{\text{a}} + \dot{E}_{\text{b}})$. As the flow gets close to **a**, it begins to again look like $\mathbf{V}_{\text{sv}}$, the trigger grows exponentially, and the cycle begins anew.

Notice that if we had not used equation (20) to determine χ, but instead used $\chi = C_3' E^{1/2} \mathcal{E}$ where C_3' is a constant, figure 2 (and our model) change qualitatively. Then, equation (34) would be replaced with

$$d\mathcal{E}/dt = C_3' E^{1/2} \mathcal{E} - C_2 \mathcal{E}/R \tag{38}$$

which has the property that $d\mathcal{E}/dt = 0$ whenever $E = (C_2/RC_3')^2$. This would make the value of E at the fixed point **c** equal to the value of E that occurs when $\mathcal{E}$ has its maximum value, since in both cases $d\mathcal{E}/dt = 0$. This is certainly

not observed in our direct numerical simulations of the Navier–Stokes equation and lends credence to our use of equation (34).

4.4 Choice of Parameters

The reason that all of the burst cycles in figure 1 are not identical (and that the points labeled as **a** in figure 1 do not exactly correspond to the crossing of the two curves *and* the minimum of the broken curve) is that the turbulence introduces stochasticity in the initial amplitude α_0 of the Floquet mode (see §3). For cycles with small α_0, the solution in figure 2 moving from **d** to **a** along the broken curve gets close to **a** before χ turns 'on' and the turbulent phase begins. When α_0 is large, χ turns 'on' before the solution reaches **a**. When that happens the solution traverses a closed path near, but completely inside, the path shown in figure 2. This implies that in figure 1, when α_0 is large, the intersection of the $\dot{E}_{\rm diss}$ and $(\dot{E}_{\rm a} + \dot{E}_{\rm b})$ curves (at low $\dot{E}_{\rm diss}$ and labeled **a**) occur at values larger than their nominal ones. (We define a cycle to be 'nominal' when $\alpha_0 \simeq 0$ and the cycle in figure 2 where the cycle gets very close to the fixed points at $E = E_0$ and $\mathcal{E} = 0$ and at $E = E_f$, $\mathcal{E} = \mathcal{E}_f$.) The same logic shows that when α_0 is large, the intersection of the solid and broken curves in figure 1 at high $\dot{E}_{\rm diss}$ labeled **c** occurs at a smaller value than its nominal one with $\alpha_0 \simeq 0$. Similarly for large α_0 the maximum values of $\dot{E}_{\rm diss}$ in figure 1 and $\mathcal{E}$ in figure 2 are smaller than their nominal values, and the minimum values of $\dot{E}_{\rm diss}$ in figure 1 and $\mathcal{E}$ in figure 2 are larger than their nominal values.

There is also stochasticity in the values of L_a and L_b (during the turbulent phase of the cycle). That stochasticity could adjust the values of E and $\mathcal{E}$ at **b** and **c** up or down, but not affect the values at **a** or **d**. Thus E_0 corresponds to the *minimum* value of all of the points labeled **a** in figure 1 (which corresponds to the cycle with the minimum value of α_0), and this is how we empirically set the value of E_0 in our model. The values of C_1 and C_2 are best set by evaluating the viscous dissipation of E and $\mathcal{E}$ from the numerical simulations and multiplying them by R/E and $R/\mathcal{E}$ respectively. We set the values of C_3 (which by stochasticity can have slightly different values for each burst cycle and, in fact, vary slightly between the turbulent and laminar phases of the same cycle) by first determining the values of E_f and $\mathcal{E}_f$ at **c** (assuming $\mathcal{E}_c \simeq \mathcal{E}_f$). Then C_3 during the turbulent phase of the burst cycle is determined from equation (36) at **c** with $\partial\mathcal{E}/\partial t \equiv 0$. This value of C_3 agrees well with computing χ from the numerical simulations via equation (12) and then solving for C_3 from equation (20). The value of C_4 is determined (using the values of C_1, C_2 and C_3) from equation (35) at **c** with $\partial E/\partial t \equiv 0$. The values of C_4 can also be computed by calculating $(\dot{E}_{\rm a} + \dot{E}_{\rm b})$ directly from the numerical simulations using equations (7) and (8) and then using equation (32) to find C_4. This value of C_4 agrees within 10% of the value found by the former method. We note that during the burst cycle C_4 (as found by the latter method) changes by less than 15% during a cycle.

4.5 Tests of the Model

Several features predicted by the model agree remarkably well with the numerical simulations. Most of the model's qualitative features are insensitive to the values of the parameters and are not due to 'parameter fitting'.

The following properties of our model are independent of order–unity changes in the parameter values (if they change by several orders of magnitude, the cycle in figure 2 will change qualitatively, i.e., $\mathcal{E}$ will not obtain a local maximum value on the path $\mathbf{a} \rightarrow \mathbf{c}$). In the absence of stochasticity, (and if the model were accurate), the full numerical simulations of the Navier–Stokes equation would also have these properties. As far as we know the full set of the properties below is not shared by other mathematical models of bursts, though, of course, some of the other models have some of the properties, [5], [6], [7].

- Our mathematical model retains two properties predicted by our physical model: the time in the laminar phase scales as $(R - R_c')^{-1}$ and the time in the turbulent phase scales independently of $(R - R_c')$. The full simulations (and laboratory observations) always have these properties. The reason that our model has these properties is that all of the coefficients of the model in equations (35) –(36) are independent of $(R - R_c')$ except R which is nearly independent of it. Only equation (37) depends on $(R - R_c')$ because β is proportional to it. Thus all time scales of the cycle in figure 2 are independent of $(R - R_c')$ except when the flow is in its laminar phase.
- At points labeled **a** (defined to be the crossing of the $(\dot{E}_\mathrm{a} + \dot{E}_\mathrm{b})$ and $\dot{E}_\mathrm{diss}$ curves that have low values of $\dot{E}_\mathrm{diss}$), the $(\dot{E}_\mathrm{a} + \dot{E}_\mathrm{b})$ curve has local minima. The full simulations in figure 1 show that this is a very good approximation.
- At **a**, E is (only approximately if α_0 is large) at its local maximum and $\mathcal{E} = 0$. The full simulations agree well with this.
- As the flow starts a turbulent burst, $\dot{E}_\mathrm{diss}$ increases faster than $(\dot{E}_\mathrm{a} + \dot{E}_\mathrm{b})$, and E decreases faster than $\mathcal{E}$ increases. This results in $\dot{E}_\mathrm{diss}$ reaching its maximum value $\dot{E}_\mathrm{diss}^\mathrm{max}$ before $(\dot{E}_\mathrm{a} + \dot{E}_\mathrm{b})$ reaches its maximum. $\mathcal{E}$ reaches its maximum value $\mathcal{E}^\mathrm{max}$ just after $\dot{E}_\mathrm{diss}$ reaches its maximum (which is defined as the location **b**) and well before E reaches its minimum. The full simulations always agree with this temporal ordering.
- At **c** (defined as the location where $(\dot{E}_\mathrm{a} + \dot{E}_\mathrm{b})$ and $\dot{E}_\mathrm{diss}$ cross with high values of $\dot{E}_\mathrm{diss}$), E has a local minimum, and $(\dot{E}_\mathrm{a} + \dot{E}_\mathrm{b})$ has a local maximum, but neither $\mathcal{E}$ nor $\dot{E}_\mathrm{diss}$ are at there maximum values. This agrees well with full simulations. If equation (20) for χ were not used and replaced with $\chi = C_3' E^{1/2} \mathcal{E}$, then $\mathcal{E}$ would have its maximum value at the fixed point **c** which is in contradiction to what is observed in the full simulations.
- The value of $(E/\sqrt{\mathcal{E}})$ is the same at **b** and **c**. The value is equal to C_2/C_3; although C_3 was determined from the numerical simulations data at **c**, no fit of parameters is used at **b**, so this is an independent test. This agrees very well with full simulations.
- After the turbulence collapses, $\dot{E}_\mathrm{diss}$ does not monotonically decrease from $\mathbf{c} \rightarrow \mathbf{a}$ but has a local minimum (labeled **d**). This is always true in the simulations.

- At **d**, $\mathcal{E} \simeq 0$. This is always true in the simulations.
- The time from **c** $\rightarrow$ **d** is set by the time scale R/C_2. This is always true in the simulations.

Additional confirmation of the model is quantitative. For each cycle, once the parameters C_3 and C_4 are determined, not only do the model's predictions of $\dot{E}_{\rm diss}(t)$ and $(\dot{E}_{\rm a}(t)+\dot{E}_{\rm b}(t))$ agree well with those of the numerical simulations over the full cycle, but so do $E(t)$ and $\mathcal{E}(t)$. This is a non–trivial result that is not pre–determined by parameter fitting.

The values of C_3 and C_4 do not have stochastic noise during the laminar phase (e.g., points **a** and **d**), therefore cycles differ during the laminar phase only due to the stochasticity in α_0. For cycles with large values of α_0, $\dot{E}_{\rm diss}$ (and $(\dot{E}_{\rm a}+\dot{E}_{\rm b})$) and $\mathcal{E}$ at **a** and **d** are larger than their nominal values, while E is smaller. This is seen in figure 1: Consider any set of two contiguous cycles. Think of the cycles beginning at **d** rather than **a**. In temporal order the points of the two cycles are: ($\mathbf{d}_1$, $\mathbf{a}_1$, $\mathbf{b}_1$, $\mathbf{c}_1$, $\mathbf{d}_2$, $\mathbf{a}_2$, $\mathbf{b}_2$, $\mathbf{c}_2$). If $\dot{E}_{\rm diss}$ at $\mathbf{d}_1$ is larger (smaller) than it is at $\mathbf{d}_2$, then from the model we infer that α_0 is larger (smaller) for the first cycle than it is for the second. We would then predict that $\dot{E}_{\rm diss}$ at $\mathbf{a}_1$ is larger (smaller) than it is at $\mathbf{a}_2$. This is confirmed in figure 1 for all cycles. Similarly (if there were no stochasticity in C_4 and C_3), the $\dot{E}_{\rm diss}$ at $\mathbf{b}_1$ would be smaller (larger) than at $\mathbf{b}_2$. While this latter relation is not always true in figure 1, it often is. For example in figure 1 we infer from the model that the flow at $0 < t < 300$ and $600 < t < 900$ where the differences between the maxima at **b** and minima at **d** in the solid $\dot{E}_{\rm diss}$ curve are large is characterized by low α_0; the flow at $300 < t < 600$ where the differences between the maxima and minima are small is characterized by large α_0.

Our model makes several new predictions that can be tested by laboratory experiments. The most striking prediction is this: when R increases, so does $\mathcal{E}_f$. We would not expect $\mathcal{E}_c$ to depend on R. Define $R_{\rm turb}$ to be the critical value at which $\mathcal{E}_f = \mathcal{E}_c$. We would expect that for $R > R_{\rm turb}$, the cycles stop and the flow remains in a permanently turbulent state. Laboratory observations confirm the existence of $R_{\rm turb}$, but the observations are not quantitative. Intuitively, one might think that the permanently turbulent state forms because its turbulence does not decay. Therefore one might think that for R just greater than $R_{\rm turb}$, the $\mathcal{E}$ of the permanently turbulent state is equal to $\mathcal{E}^{\rm max}$ (the value at **b**). Instead, our model predicts that $\mathcal{E}$ would have the much smaller value of $\mathcal{E}_f$. This would be a useful laboratory test.

Another test is provided by measuring $T_{\rm L}$ and $T_{\rm B}$ as functions of R as $R \rightarrow R_{\rm turb}$. There are three ways in which the flow can make the transition from burst cycles to a state of permanent turbulence: (i) $T_{\rm L} \rightarrow 0$ and $T_{\rm B}$ remains finite and nearly independent of $(R_{\rm turb} - R)$; (ii) $T_{\rm L} \rightarrow 0$ and $T_{\rm B} \rightarrow \infty$; or (iii) $T_{\rm L}$ remains finite and nearly independent of $(R_{\rm turb} - R)$ and $T_{\rm B} \rightarrow \infty$. Our model predicts (iii), which could be easily verified in the laboratory. In addition, our model predicts that $T_{\rm B}$ scales as $ln(R_{\rm turb} - R)$ as $R \rightarrow R_{\rm turb}$. This scaling would be difficult to verify if there were much stochasticity in C_3, C_4 or α_0.

The work at UCB was supported by NSF–CTS–8906343. Computations were done at the San Diego Supercomputer Center through an NPACI award.

References

1. COUGHLIN, K. & MARCUS, P. S. 1996 Turbulent bursts in Couette-Taylor flow. *Phys. Rev. Lett.* **77** 2214–2217.
2. COUGHLIN, K., HAMILL, C. F., MARCUS, P. S. & SWINNEY, H. L. 1999 Turbulent bursts in Couette-Taylor flow. *Journal of Fluid Mechanics* under review.
3. ANDERECK, C. D., LIU, S. S. & SWINNEY, H. L. 1986 Flow regimes in a circular Couette system with independently rotating cylinders. *J. Fluid Mech.* **164**, 155-183.
4. HAMILTON J. M., KIM, J. & WALEFFE, F. 1995 Regeneration mechanisms of near-wall turbulence structures. *J. Fluid Mech.* **287**, 317-348.
5. BAGGETT, J. S. & TREFETHEN, L. N. 1997 Low-dimensional models of subcritical transition to turbulence. *Phys. Fluids* **9**, 1043-1053.
6. AUBRY, N., HOLMES, P., LUMLEY, J. & STONE, E. 1988 The dynamics of coherent structures in the wall region of a turbulent boundary layer. *J. Fluid Mech.* **192**, 115-173.
7. WALEFFE, F. 1995 Hydrodynamic stability and turbulence - beyond transients to a self-sustaining process. *Stud. App. Math.* **95**, 319-343.